Eleventh International Conference on Computational Fluid Dynamics (ICCFD11), Maui, HI, USA, July 11-15, 2022

ICCFD11-2022-1602

A shock capturing subfilter scale Legendre spectral viscosity (LSV) closure applied to high-order flux reconstruction schemes

V. C. B. Sousa* and C. Scalo*,**
Corresponding author: vsousa@purdue.edu

* School of Mechanical Engineering, Purdue University, USA
** School of Aeronautics and Astronautics, Purdue University, USA

Abstract: The mathematical formalism of the filtered governing equations is applied as an approach for shock capturing in high-order flux reconstruction schemes. Such perspective has been popularized for turbulence modeling in the context of Large-Eddy Simulations (LES) but its applicability to simulations of flow discontinuities have not yet been fully explored. Within this background, the Legendre Spectral Viscosity (LSV) subfilter scale (SFS) closure model, capable of performing simulations in the presence of shock-discontinuities, is introduced. The LSV method exploits the set of hierarchical basis functions formed by the Legendre polynomials to extract the information on the energy content near the resolution limit and estimate the overall magnitude of the required SFS dissipative terms, resulting in a scheme that dynamically activates only in cells where nonlinear behavior is important. Additionally, the modulation of such terms in the Legendre spectral space allows for the concentration of the dissipative action at small scales. The proposed method is tested in canonical shock-dominated flow setups in both one and two dimensions. These include the 1D Burgers' problem, a 1D shock tube, a 1D shock-entropy wave interaction and a 2D inviscid shock-vortex interaction. Results showcase a high-degree of resolution power, achieving accurate results with a small number of degrees of freedom, and robustness, being able to capture shocks associated with the Burgers' equation and the 1D shock tube within a single cell with orders 120 and higher. The content of this manuscript is taken from the published article by Sousa and Scalo (2022a).

Keywords: Shock capturing, High-Order methods, Flux-Reconstruction, Spectral Viscosity.

1 Introduction

In recent years, considerable effort has been put into the development of discontinuous high-order methods capable of solving a wide range of PDE's, including the Navier-Stokes equations. Such methods display a high convergence rate and, in general, require smaller grid resolutions to achieve accurate results when compared to the low-order counterpart. The latter, however, are more robust due to the inherent dissipation embedded in the low-order numerics. The presence of high-gradients in the computational domain, such as shock-induced discontinuities, is particularly challenging for high-order schemes and dissipation must be introduced to avoid numerical instabilities. Nonetheless, this step must be performed meticulously so that the large scales present are minimally affected. A careless introduction of a dissipation term to stabilize a shock could deteriorate a large band of the spectrum of resolvable turbulence when both phenomena happen concomitantly, for example.

Although modeling approaches for hydrodynamic turbulence and shock formation have taken historically different paths, both phenomena are characterized by an energy cascade from large to small scales due to nonlinear interactions (Frisch, 1995; Gupta and Scalo, 2018). Therefore, their numerical simulation could

be treated in a similar fashion, that is by solving the filtered compressible Navier-Stokes equations. In the context of finite-difference solvers, a closure capable of performing both tasks was recently developed by Sousa and Scalo (2022b). The current work is the first step towards extending the previously developed method for high-order discontinuous flux reconstruction (Huynh, 2007) methods that can be used in unstructured grid solvers. It uses the Large Eddy Simulation (LES) framework, based on solving the filtered quantities and modeling of the subfilter scale (SFS) energy flux, to capture any discontinuity present in the flow through a closure model obtained via a projection of the discontinuous solution within each element onto the set of Legendre basis functions in order to inform the magnitude of the dissipation and to modulate its strength at different scales (Sousa and Scalo, 2022a).

The flux reconstruction (FR) method (Huynh, 2007) is built upon a generalized framework that encompasses both the discontinuous Galerkin (DG) method (Cockburn and Shu, 1989; Bassi and Rebay, 1997) and the staggered-grid approach (Kopriva and Kolias, 1996). The first projects the solution vector onto test functions and applies the summation by parts rule to get to a weak form of the conservation equations where the boundary terms are substituted by the numerical upwind flux. The second solves the differential form of the conservation laws by using Lagrange polynomials and its properties to perform derivations and interpolations. It is named staggered-grid approach because it stores solution values at the Gauss quadrature points and flux values at the Gauss-Lobatto quadrature points. The latter include the points at the cell interface and its values are used to get the unique numerical flux between two cells. Despite their differences, both methods can be generalized through defining a generic correction function, g, that has unitary value at one interface and zero at the others. The correction function is then scaled by the difference between the discontinuous flux value interpolated from the interior points and the common numerical upwind flux at each of the interfaces in order to construct a continuous flux. The divergence of the continuous flux is used to advance the solution in time.

As previously mentioned, high-order methods suffer from numerical instabilities in the presence of high gradients, such as shocks. To simulate those types of flows mainly two types of strategies were developed: either use a nonlinear limiter to control the solution or add an artificial dissipation term, both active only in the vicinity of a discontinuity. In the first category are the weighted essentially non-oscillatory (WENO) type schemes (Qiu and Shu, 2005; Zhu et al., 2008; Luo et al., 2007), which constrain the solution to being non-oscillatory near discontinuities with high-order stencils. Such limiters have been successful in some applications but they are known to induce over dampening of physical fluctuations near discontinuities (Haga and Kawai, 2019).

The other strategy is related to the addition of artificial viscosity, which increases the physical dissipation mechanisms with a term proportional to the flow gradients with the objective to enlarge the thickness of eventual discontinuities ultimately rendering them resolvable at a certain grid resolution. Recently, the Local Artificial Diffusivity (LAD) scheme, also based on artificial viscosity and initially developed for high order finite difference methods (Cook, 2007; Kawai and Lele, 2008; Kawai et al., 2010) was extended to the spectral difference staggered-grid method (Premasuthan et al., 2014) and to the FR approach (Haga and Kawai, 2019). Most notably, the FR-LAD method was able to outperform FR-WENO schemes in a shock-entropy wave interaction problem with respect to resolving the trailing small scale waves in the density field. Moreover, Haga and Kawai (2019) also showed a LES of an overexpanded supersonic jet displaying the capability of the method for engineering applications. Despite these results, the FR-LAD approach showed some drawbacks: first, it is limited to polynomial orders of degree 4; second, its implementation requires a smoothing filter performed through a computationally intensive restriction-prolongation operation.

In parallel, the Spectral Vanishing Viscosity (SVV) method was developed for single elements with spectral discretization based on Fourier (Tadmor, 1989, 1990) and Legendre (Maday et al., 1993) basis functions with the pretense of recovering spectral convergence properties when solving conservation laws that form shock discontinuities spontaneously. This method consists of adding a convolution kernel to the artificial dissipation term, i.e. a wavenumber-dependent viscosity term, concentrating its action at the small scales near the resolution limit with the objective to prevent oscillations and lead to convergence to the unique entropy solution. Initially, it was shown by mathematical proofs and numerical experiments that a sharp viscosity activation after a certain wavenumber was successful in achieving the aforementioned stability goals (Tadmor, 1989) but further study by Maday et al. (1993) showed an increased performance if a smooth convolution kernel was used. In an attempt to extend the SVV methodology to FR methods, Asthana et al. (2015) first proved that the addition of adequate artificial dissipation can ensure nonlinear stability and chose

to implement the needed dissipation as the result of a filtering operation in Fourier space via convolution. Being the convolution operation nonlocal, the elementwise solution was padded with information from its neighbors and it was argued that this was critical to stabilizing inter-element discontinuities. The proposed formulation was shown to be able to solve a 1D Burgers problem with polynomial order as high as 119 and to solve problems related to the 1D Euler equations up to order 8.

In the analysis presented in Sousa and Scalo (2022b), the authors showed that a low-band filtering of a nonlinear conservation law leads to a wavenumber dependent subfilter flux term, therefore, the artificial addition of such dissipation terms on previous publications were akin to performing simulations of the filtered governing equations but without exploiting some of the physical aspects of this consideration. Furthermore, Sousa and Scalo (2022b) explored the similarities between the theoretically expected wavenumber-dependent eddy viscosity obtained via studying turbulence spectra (Kraichnan, 1976; Chollet and Lesieur, 1981) and the one obtained via studying discontinuous solutions of the Burgers' and Euler equations to develop a single mathematical framework for capturing shocks and subfilter turbulence concomitantly. The current manuscript is a step towards extending the methodology developed in Sousa and Scalo (2022b) to discontinuous discretization schemes that can be used in unstructured solvers. It leverages the Legendre polynomials, a hierarchical basis functions symbiotic to the implementation of FR schemes, to estimate the kinetic energy at the smallest resolvable scale to dynamically inform the magnitude of the dissipation needed and to modulate the dissipation in the Legendre spectral space.

The Legendre Spectral Viscosity (Sousa and Scalo, 2022a) method's implementation and results are summarized in the current manuscript. Shock dominated problems in one and two dimensions are addressed showcasing the performance of the proposed method in discontinuity capturing in high-order discontinuous scheme settings. Although, the presented methodology is theoretically able to model turbulence and shocks concomitantly, in the example of Sousa and Scalo (2022b), three-dimensional problems encompassing shocks, turbulence and their interaction are left for a future work.

2 Flux reconstruction methodology

In this section the filtered compressible Navier-Stokes equations will be presented together with a description of the subfilter scale terms, all within the context of high-order Flux Reconstruction (FR) (Huynh, 2007) methods. The proposed LSV closure, which possesses shock-capturing capabilities, is addressed later, in section 3.

2.1 Grid transformation

In a discontinuous numerical discretization, the computational domain (Ω) is subdivided into non-overlapping elements (Ω_k) such that

$$\Omega = \bigcup_k \Omega_k. \tag{1}$$

Each individual cell is then mapped through an invertible relation from the physical cartesian coordinate system, $\mathbf{x} = (x^1, x^2, x^3)$, onto a standard element $\tilde{\Omega} := \{\xi^i | -1 \leqslant \xi^i \leqslant 1\}$ for $i = 1, 2$ and 3. Note that this definition is only viable for hexahedral cells, which the current work chooses to focus on. Flux reconstruction implementations on triangles and prisms can be found in Wang and Gao (2009) and Williams et al. (2013).

Moving forward, if a generalized curvilinear grid transformation is used and the resulting equations are filtered in the reference space, one reaches the curvilinear compressible filtered Navier-Stokes equations. These, together with the aforementioned simplifications, can be written in the standard element coordinates, $\xi = (\xi^1, \xi^2, \xi^3)$, as

$$\frac{\partial \overline{J\rho}}{\partial t} + \frac{\partial}{\partial \xi^j}\left(\overline{J\rho}\check{v}^j\right) = 0, \tag{2}$$

$$\frac{\partial \overline{J\rho}\check{v}^i}{\partial t} + \frac{\partial}{\partial \xi^j}\left(\overline{J\rho}\check{v}^i\check{v}^j + \overline{Jp}g^{ij} - J\check{\sigma}^{ij} + \overline{J\rho}\tau^{ij}\right) = -\Gamma^i_{qj}\left(\overline{J\rho}\check{v}^q\check{v}^j + \overline{Jp}g^{qj} - J\check{\sigma}^{qj} + \overline{J\rho}\tau^{qj}\right), \tag{3}$$

$$\frac{\partial \overline{JE}}{\partial t} + \frac{\partial}{\partial \xi^j}\left(\overline{J(E+p)}\check{v}^j + J\check{Q}^j - J\check{\sigma}^{ij}g_{ik}\check{v}^k + \frac{1}{2}\left(\frac{\gamma\pi^j}{\gamma-1} + \overline{J\rho}C_p q^j\right)\right) = 0. \tag{4}$$

The important nonlinear terms that contribute to the energy flux from large to small scales are, the SFS stress tensor,

$$\tau^{ij} = \widetilde{v^i v^j} - \check{v}^i\check{v}^j, \tag{5}$$

the SFS heat flux,

$$q^j = \widetilde{Tv^j} - \check{T}\check{v}^j, \tag{6}$$

and the SFS pressure-work,

$$\pi^j = \overline{pv^j} - \overline{p}\check{v}^j. \tag{7}$$

Similar equations were first introduced by Jordan (1999) who developed the incompressible LES methodology in generalized curvilinear coordinates which were then expanded to the compressible version by Nagarajan et al. (2007). In previous literature though, an arbitrary choice was made to model the subfilter components emanating from the nonlinear advection of the total energy and pressure as proportional to a subfilter heat flux. Although this is an appropriate interpretation given the correct scaling, there is an advantage for including both the SFS pressure-work and heat flux into the formulation. This stems from the fact that a smooth temperature field does not imply the same property to the pressure field and vice-versa. Furthermore, since the gradient of a field acts as a sensor for high wavenumbers and, being the SFS contributions generally modeled as being proportional to the gradient of the field they are related to, using only the temperature field would render the final model essentially blind to spurious oscillations in the pressure field. Ultimately, the formulation in equation (4) averages the contributions to subfilter scales that would arise if only the pressure or the temperature field were being used in the modeling process. This way, in theory, no additional dissipation is added into the system of equations but the SFS terms are now able to sense high-wavenumber build up on both the pressure and temperature fields.

In the aforementioned relations, J is the Jacobian of the transformation which is the determinant of the Jacobi matrix ($J_{ij} = \partial x^i/\partial\xi^j$), the velocity vector is mapped, $v^i = \frac{\partial\xi^i}{\partial x^j}u^j$, and the Favre filtering is defined as being,

$$\check{f} = \frac{\overline{J\rho f}}{\overline{J\rho}}. \tag{8}$$

Moreover, the tensors accounting for a general curvilinear mapping of the physical element to the euclidean standard cell are the covariant and contravariant metric tensors

$$g_{ij} = \frac{\partial x^i}{\partial\xi^k}\frac{\partial x^j}{\partial\xi^k}, \quad g^{ij} = \frac{\partial\xi^k}{\partial x^i}\frac{\partial\xi^k}{\partial x^j}, \tag{9}$$

respectively, and the Christoffel symbol of the second kind,

$$\Gamma^i_{qj} = \frac{\partial\xi^i}{\partial x^l}\frac{\partial^2 x^l}{\partial\xi^q\partial\xi^j}. \tag{10}$$

In the derivation of these equations, the metric tensors and Christoffel symbols are assumed to be varying slowly over the spatial support of the filter kernel, therefore leading to no additional subfilter flux terms.

Ultimately, following the inner product rules and the transformations between covariant and contravariant vector components in the space of the nonorthogonal spatially varying basis functions, the viscous stress tensor and the heat flux vector are described by

$$\frac{\overline{Jp}}{\gamma-1} = \overline{JE} - \frac{1}{2}\overline{J\rho}g_{ij}\check{v}^i\check{v}^j - \frac{1}{2}\overline{J\rho}g_{ij}\tau^{ij}, \tag{11}$$

$$\check{\sigma}^{ij} = \mu \left(g^{jk} \frac{\partial \check{v}^i}{\partial \xi^k} + g^{ik} \frac{\partial \check{v}^j}{\partial \xi^k} - \frac{2}{3} g^{ij} \frac{\partial \check{v}^k}{\partial \xi^k} \right), \tag{12}$$

$$\check{Q}_j = -k g^{ij} \frac{\partial \check{T}}{\partial \xi^i}. \tag{13}$$

The complete generic system of equations that is originated from a curvilinear mapping of a physical element to a standard cell is reported here for the sake of completeness. In practice some simplifying assumptions can be applied to the governing equations. If, for example, a linear mapping is assumed between the physical and standard elements, then the Christoffel symbols are all equal to zero due to the second derivative term present in its definition (10). Furthermore, if the transformation is assumed to be orthogonal, then all the off-diagonal terms of the metric tensors g_{ij} and g^{ij} will also be trivially zero. In that case, the transformation is reduced to a simple scaling of the element. In fact, in 1D, the whole transformation can be condensed into a single factor calibrating the derivatives, as show in Huynh (2007).

2.2 Numerical discretization of a reference element

The conservation equations in the frame of reference of the standard element are then discretized within each cell by a set of solution points. This allows high-order accuracy calculations within the element, for example a N-th order polynomial interpolation can be achieved by using the product of $N+1$ points in each coordinate direction. Since a three-dimensional cell can be simply described by an outer product of 1D discretizations in each direction, the discussion hereafter will be focused on the simpler case.

Now, take $u \in P_N$, the space of N-th order polynomials, as an approximation of an unknown quantity U. Let $\{h_j(\xi)\}_{j=0}^N$ be the set of Lagrange polynomials associated with the Gauss-Legendre quadrature points $\{\xi_j\}_{j=0}^N$. The quadrature nodes, for this case, are defined as being the zeros of $L_{N+1}(\xi)$, where $L_N(\xi)$ is the N-th order Legendre polynomial. Shen et al. (2011) describes an efficient algorithm to compute the location of the interior nodes of the Legendre-Gauss by finding the eigenvalues of the following matrix,

$$A_{N+1} = \begin{bmatrix} 0 & \sqrt{b_1} & \dots & & 0 \\ \sqrt{b_1} & 0 & \sqrt{b_2} & & \vdots \\ \vdots & \ddots & \ddots & \ddots & \\ & & \sqrt{b_{N-1}} & 0 & \sqrt{b_N} \\ 0 & & \dots & \sqrt{b_N} & 0 \end{bmatrix}, \tag{14}$$

where,

$$b_i = \frac{i^2}{4i^2 - 1}. \tag{15}$$

This set of points are chosen since they influence the stability of the system by decreasing the importance of the Runge's phenomenon (Karniadakis and Sherwin, 2013) and minimizing aliasing errors in nonlinear flux reconstruction schemes (Jameson et al., 2012). Then,

$$u(\xi) = \sum_{j=0}^{N} u(\xi_j) h_j(\xi). \tag{16}$$

Clearly, differentiating $u(\xi)$ m times just means evaluating the m-th derivative of the Lagrange polynomials, $\{h_j^{(m)}(\xi)\}_{j=0}^N$. This operation can be further simplified to be efficiently numerically implemented. Shen et al. (2011) has proved that the collocated m-th derivative can be computed as the m-th power of D, the matrix representation of the first-order derivative operation. The entries of D,

$$D_{ij} = \begin{cases} \frac{L'_{N+1}(\xi_i)}{L'_{N+1}(\xi_j)} \frac{1}{\xi_i - \xi_j}, & \text{if } i \neq j, \\ \frac{\xi_i}{1-\xi_i^2}, & \text{if } i = j, \end{cases} \tag{17}$$

associated to the Gauss-Legendre quadrature points can be determined by the using the Legendre polynomials (L_n), which obey the following recurrence relations

$$(n+1)L_{n+1}(\xi) = (2n+1)\xi L_n(\xi) - nL_{n-1}(\xi), \tag{18}$$

$$(1-\xi^2)L'_n(\xi) = \frac{n(n+1)}{2n+1}\left(L_{n-1}(\xi) - L_{n+1}(\xi)\right), \tag{19}$$

for $n \geqslant 1$ and with $L_0 = 1$. Ultimately the collocated derivative operation is defined as

$$u^{(m)}(\xi_i) = D^m_{ij}\ u(\xi_j), \tag{20}$$

where D^m is the m-th power of the derivation matrix.

At this point the particularities of the Flux Reconstruction (FR) scheme start. The governing equations for the standard element (2)-(4) are cast in the format of the divergence of a flux. The formulation of an inherently conservative scheme needs the flux vector to be identical at interfaces between neighboring cells. Since the FR scheme relies on independent discontinuous cells to work, the interpolated flux values from neighboring cells at the common interfaces are different in general. The flux discontinuity is addressed by defining a numerical flux function. In the current work the Lax-Friedrichs flux was used, which retains a positivity-preserving property when applied to the compressible Euler equations (Zhang, 2017). The common value is then used to correct the initially discontinuous flux functions in each cell and the divergence is taken.

The distinction of the FR scheme relies on how such correction procedure is performed. Now consider a 1D formulation and let $f_k \in P_N$ be the approximation of the flux vector F within the k-th cell. The interpolated value from the solution points to the cell interfaces can be evaluated at the cells' interfaces via,

$$f_k(\pm 1) = \sum_{j=0}^{N} f_k(\xi_j) h_j(\pm 1). \tag{21}$$

These values, as well as the ones obtained from neighboring cells, $f_{k-1}(+1)$ and $f_{k+1}(-1)$ in this example, are used as inputs for the numerical flux function which outputs a unique flux value at each respective interface,

$$f^{un}_{k-\frac{1}{2}} = \text{Numerical Flux}\left[f_{k-1}(+1), f_k(-1)\right], \quad f^{un}_{k+\frac{1}{2}} = \text{Numerical Flux}\left[f_k(+1), f_{k+1}(-1)\right]. \tag{22}$$

Although various numerical flux strategies can be used in this step, the Lax-Friedrichs flux was adopted and its one dimensional version is presented hereafter for completeness:

$$f^{un}_{k-\frac{1}{2}} = \frac{f_{k-1}(+1) + f_k(-1) - a_{k-1,k}(U_k - U_{k-1})}{2}, \quad f^{un}_{k+\frac{1}{2}} = \frac{f_k(+1) + f_{k+1}(-1) - a_{k,k+1}(U_{k+1} - U_k)}{2}. \tag{23}$$

Here, U is the conserved variable related to the corresponding flux value f and $a_{\cdot,\cdot}$ is the maximum eigenvalue of the Jacobian matrix $|\frac{\partial f}{\partial U}|$ taken at a cell interface. This value is equal to the magnitude of the normal velocity crossing said interface augmented by the speed of sound, that is,

$$a_{k-1,k} = \max_{i=k-1,k}\left(|v^1_i(\pm 1)| + \sqrt{\frac{\gamma p_i(\pm 1)}{\rho_i(\pm 1)}}\right), \quad a_{k,k+1} = \max_{i=k,k+1}\left(|v^1_i(\pm 1)| + \sqrt{\frac{\gamma p_i(\pm 1)}{\rho_i(\pm 1)}}\right), \tag{24}$$

when a perfect gas equation of state is considered. In higher dimensions the maximum operation is taken across all the points at a given cell interface and the velocity vector is dotted with the normal component of said interface. A detailed summary of a multidimensional implementation of such a flux, together with a description on its weak positivity property when applied to the Euler equations in high-order schemes, can be found in (Zhang, 2017). Other possible choices for the flux function include the Godunov (Godunov and Bohachevsky, 1959) or HLLC flux schemes (Harten et al., 1983; Toro et al., 1994; Batten et al., 1997).

At this point, the FR scheme introduces correction functions for the left (g_L) and right (g_R) boundaries (Huynh, 2007). These correction functions are defined as symmetric $(N+1)$th-order polynomials, i.e. $g_R(\xi) = -g_L(-\xi)$, that satisfy the boundary conditions $g_L(-1) = 1$ and $g_L(+1) = 0$. These properties allow

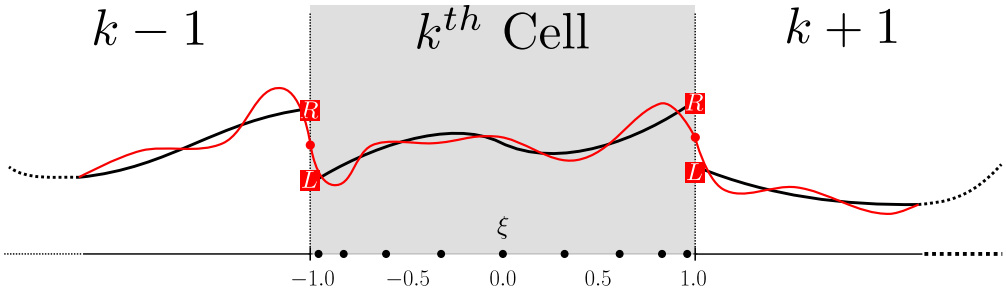

Figure 1: One dimensional schematic of a the construction of a continuous flux function, in red, by correcting the initially discontinuous field (black) via high-order correction functions, g_L and g_R and enforcing it to be equal to the solution of a numerical flux function at the interface.

the construction of a continuous flux function f_k^c, see schematic in figure 1, by modifying the values at the interfaces as

$$f_k^c(\xi) = f_k(\xi) + \left(f^{un}_{k-\frac{1}{2}} - f_k(-1)\right) g_L(\xi) + \left(f^{un}_{k+\frac{1}{2}} - f_k(+1)\right) g_R(\xi). \tag{25}$$

The divergence of the continuous flux at the solution points $\{\xi_i\}_{i=0}^N$ needed to advance the solution in time is then obtained

$$\left.\frac{\partial f_k^c}{\partial \xi}\right|_{\xi=\xi_i} = D_{ij} f_k(\xi_j) + \left(f^{un}_{k-\frac{1}{2}} - f_k(-1)\right) g_L'(\xi_i) + \left(f^{un}_{k+\frac{1}{2}} - f_k(+1)\right) g_R'(\xi_i). \tag{26}$$

Huynh (2007) suggested various polynomials to be used as correction functions. For example, if the right Radau polynomial,

$$R_{R,N+1} = \frac{(-1)^{N+1}}{2}\left(L_{N+1} - L_N\right), \tag{27}$$

is used as g_L, then the scheme becomes equivalent to the nodal DG scheme for linear problems. With this in mind, Huynh (2007) denominated this polynomial as $g_{DG,N+1}$. Other suitable correction functions were also presented, such as

$$g_{Ga,N+1} = \frac{N+1}{2N+1} R_{R,N+1} + \frac{N}{2N+1} R_{R,N}, \tag{28}$$

$$g_{2,N+1} = \frac{N}{2N+1} R_{R,N+1} + \frac{N+1}{2N+1} R_{R,N}. \tag{29}$$

The use of different correction functions render different accuracy and stability properties to the scheme. Among these, g_{DG} is the most accurate but also the one with the biggest constraint on time step size. These properties are inverted for g_2. Being a good compromise, g_{Ga}, shown in figure 2, is adopted in the current work. Similar motives also led Haga and Kawai (2019) to choose g_{Ga} as a correction function.

3 Legendre Spectral Viscosity (LSV) closure models

The filtered compressible Navier-Stokes system of equations require a subfilter scale (SFS) model to be closed. With only information on the large scales of the conserved variables, it is not possible to exactly derive an expression for the SFS terms τ^{ij} (5), q^j (6) and π^j(7) , which need to be estimated based on their corresponding resolved field.

Based on previous literature on spectral eddy viscosity models for LES (Kraichnan, 1976; Chollet and Lesieur, 1981) and spectral artificial viscosity models for shock capturing (Tadmor, 1989, 1990), a method capable of performing both tasks simultaneously, the Quasi-Spectral Viscosity (QSV) closure, was developed

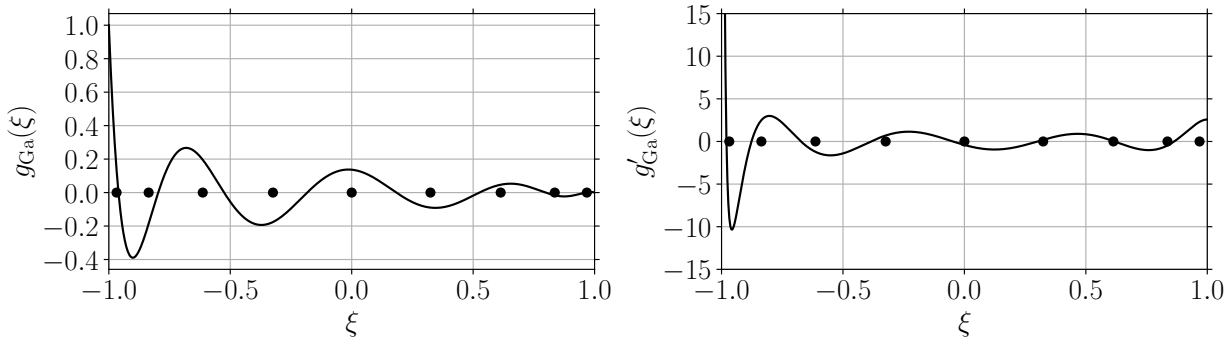

Figure 2: Example of the left correction function g_{Ga} and its derivative g'_{Ga} when $N = 8$. The Legendre-Gauss quadrature points, $\{\xi_j\}_{j=0}^{8}$, are also shown.

by Sousa and Scalo (2021). Although QSV was developed to be used in high-order finite difference methods in structure grids, the logic behind it is still useful in the current discontinuous flux reconstruction application.

The two steps for implementing the QSV method were, first, estimating the cutoff energy, E_N, and second, introducing a wavenumber dependency capable of concentrating the dissipation near the filter cutoff. The same steps are performed in the current implementation with the difference that, instead of using a Fourier basis to project the solution, a Legendre basis functions is used to estimate E_N and modulate the spectral viscosity. The operations in the Legendre space required to perform these tasks are introduced in section 3.1. The complete set of steps required for implementing the LSV closure are discussed in section 3.2. Additionally, a deeper analysis of the spectral modulation procedure is given in section 3.3.

Two important advantages of using the Legendre polynomials in discontinuous FR methods should be mentioned: first, the periodicity constraint related to Fourier modes is relaxed and local operations within each discontinuous cell can be performed; second, it is synergic, since the implementation of FR method is already based on Legendre polynomials, as discussed in section 2.2. Additionally, Maday et al. (1993) analyzed the Burgers' equation in the context of a Legendre pseudo-spectral method and proved that the use of a wavenumber-dependent viscosity concentrated near the highest resolvable mode led to convergence to the exact entropy solution.

3.1 Legendre Space Projection and Filtering

The energy at the cutoff estimation and the modal dissipation modulation depend on the Legendre transform operation, i.e. the projection of the solution onto the hierarchical Legendre modes. This operation can be performed using the information stored on the solution points due to the exactness of the Legendre-Gauss-type quadrature,

$$\langle p, 1\rangle = \int_{-1}^{1} p(\xi) d\xi = \sum_{j=0}^{N} p(\xi_j) w_j, \tag{30}$$

which hold for any polynomial that belongs to the polynomial space P up to order $2N + 1$. Here,

$$w_j = \frac{2}{(1-\xi_j^2)[L'_{N+1}(\xi_j)]^2}, \tag{31}$$

are the Gauss quadrature weights defined for each node $\{\xi_j\}_{j=0}^{N}$. This information allows the calculation of the forward discrete Legendre transform ($\mathcal{L}$),

$$\tilde{u}_n = \mathcal{L}[\mathbf{u}] = \frac{\langle u, L_n\rangle}{\|L_n\|^2} = \frac{1}{\gamma_n} \sum_{j=0}^{N} u(\xi_j) L_n(\xi_j) w_j, \tag{32}$$

where $\gamma_n = \frac{2}{2n+1}$, through which the magnitude of the hierarchical modes ($\tilde{u}_n$) are found. We now define

and a *modulated* backward discrete Legendre transform,

$$\mathcal{L}^{-1}[\sigma, \tilde{\mathbf{u}}] = \sum_{n=0}^{N} \sigma\left(\eta\right) \tilde{u}_n L_n(\xi_j), \tag{33}$$

where $\eta = n/N$, through which the modulated values in physical space can be recovered. A generic modulation function, $\sigma\left(\eta\right)$ is construed such that it is nonzero only for $0 \leqslant \eta \leqslant 1$, therefore depending only on the resolved wavenumbers. This characteristic will allow it to be used in the current work to control the spectral behavior of the added sub filter flux models.

Additionally, note that the simple choice of restricting the Legendre modal expansion up to N modes with $\sigma\left(n/N\right) = 1$ for all n modes is equivalent to a sharp spectral Legendre filtering operation of a general function $u(\xi)$ to P_N, the space of polynomials of order up to N, as displayed in figure 3. This corresponds to the primary filter operation used in the derivation of the compressible filtered Navier-Stokes equations (2) - (4) when applied to the current flux reconstruction context. Moreover, if $u(\xi) \in P_N$ and $\sigma\left(n/N\right) = 1 \; \forall \; n$, then the discrete forward and backward Legendre transforms are the inverse of one another.

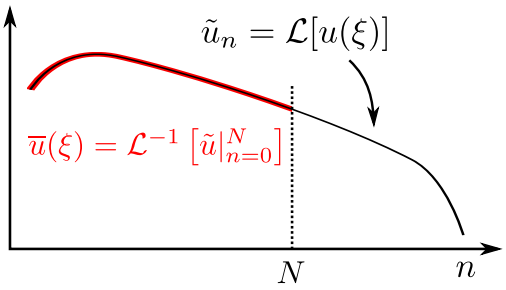

Figure 3: Schematic illustration of a sharp spectral Legendre filtering operation. The horizontal axis indicates the Legendre mode number (not the Fourier-mode wavenumber).

Although these operations seem computationally intensive, given that $L_n(\xi_j)$ $j, n = 0, 1, ..., N$ are pre-computed, the transforms can be carried out by a matrix multiplication in N^2 operations. Ultimately, a Legendre modulation operation is defined as a composition between a forward and a backwards transform

$$\mathcal{M}[\sigma, \mathbf{u}] = \mathcal{L}^{-1}[\sigma, \mathcal{L}[\mathbf{u}]], \tag{34}$$

where σ is a generic Legendre space modulation function, similar to the Fourier space filters defined in Gottlieb and Shu (1997).

3.2 Implementation of the Legendre Spectral Viscosity (LSV) closure

Moving ahead, the closure models for the system of equations (2)-(4) is addressed. First, the estimated cutoff energy for the $\overline{v}^j$ velocity component, $E_N^i(\overline{v}^j)$, can be recovered in the i-th direction by taking the forward Legendre transform of the kinetic energy field and storing the magnitude of the last mode,

$$E_N^i\left(\check{v}^j\right) = \left| \frac{1}{\gamma_N} \sum_{k=0}^{N} \frac{1}{2} (\check{v}^j(\xi_k^i))^2 L_N(\xi_k^i) w_k \right|, \tag{35}$$

which, in turn, can be used to estimate the subfilter velocity scale, $v^i(\check{v}^j) = \sqrt{\frac{N}{2} E_N^i\left(\check{v}^j\right)}$, where the pre-factor $N/2$ is the average grid spacing in the standard cell. This term, together with information on the local subcell grid spacing, approximated by the each node's quadrature weight and used to estimate the subfilter length scale (ℓ^i), is adopted to inform the magnitude of the needed dissipation,

$$\mathcal{D}^{ij} = v^i(\check{v}^j)\ell^j, \tag{36}$$

in the subfilter flux closure models. Moreover, in one dimension, the recovered information on the energy of

the last mode is constant throughout a cell. A similar behavior is desirable in higher dimension formulations to mitigate spurious oscillations. With that in mind, a maximum operation is performed between the values for the energy at the cutoff obtained at different planes in a singular cell.

At this point, the background necessary to introduce the sub-filter scale (SFS) flux closure models is covered. They are written as,

$$\tau^{ij} = -\mathcal{M}\left[\sigma_e, \frac{\delta^i_{\alpha\beta}\delta^j_{\gamma\eta}}{2}\left(\mathcal{D}^{\alpha\gamma}\frac{\partial\check{v}^\beta}{\partial\xi^\eta} + \mathcal{D}^{\gamma\alpha}\frac{\partial\check{v}^\eta}{\partial\xi^\beta}\right)\right], \tag{37}$$

$$q^j = -\mathcal{M}\left[\sigma_e, \delta^j_{\alpha\beta}\mathcal{D}^{\alpha\beta}\frac{\partial\check{T}}{\partial\xi^\beta}\right], \tag{38}$$

$$\pi^j = -\delta^l_{\alpha\beta}\mathcal{D}^{\alpha\beta}\frac{\partial\overline{p}}{\partial\xi^\beta}. \tag{39}$$

where

$$\delta^l_{\alpha\beta} = \begin{cases} 1 & \text{if} \quad l=\alpha=\beta, \\ 0 & \text{otherwise.} \end{cases} \tag{40}$$

Alternatively, the aforementioned expressions can be also written without the assumption of an implicit summation. It is written hereafter,

$$\tau^{mn} = -\mathcal{M}\left[\sigma_e, \frac{1}{2}\left(\mathcal{D}^{mn}\frac{\partial\check{v}^m}{\partial\xi^n} + \mathcal{D}^{nm}\frac{\partial\check{v}^n}{\partial\xi^m}\right)\right], \tag{41}$$

$$q^n = -\mathcal{M}\left[\sigma_e, \mathcal{D}^{nn}\frac{\partial\check{T}}{\partial\xi^n}\right], \tag{42}$$

$$\pi^n = -\mathcal{D}^n\frac{\partial\overline{p}}{\partial\xi^n}, \tag{43}$$

with no summation intended for the m and n indices. This is a clarification on the notation used in Sousa and Scalo (2022a).

Here, σ_e is the chosen modulation transfer function (see figure 4) used to decrease the dissipation added to low wavenumbers, i.e. large scales, in the SFS stress tensor and in the SFS heat flux. The SFS pressure-work, in turn, is not modulated in the current formulation because a higher level of numerical stability, necessary when solving strong shocks, was achieved. In practice, the low wavenumber pressure dissipation helped control pressure undershoots and maintain is positivity. With the help of *a priori* analysis of 1D shock dominated flows the curve,

$$\sigma_e(\eta) = 0.2 + 0.8\frac{e^{4\eta}-1}{e^4-1}, \tag{44}$$

was adopted. Although this modulation transfer function has been used successfully in numerical experiments reported in the current manuscript, it is not optimized. Additional discussion on the modulation transfer function and the *a priori* analysis is provided hereafter in section 3.3.

Moving forward, the last step in the implementation of the closure models in a discontinuous flux reconstruction setting is taking the derivatives related to the SFS modeling accounting for the discontinuity of the solution across neighboring cells. This step is applicable to the divergence of all the modeled sub-filter scale flux terms. As an example, the divergence of the SFS heat flux,

$$\left.\frac{\partial q^l_k}{\partial\xi}\right|_{\xi=\xi_i} = D_{ij}q^l_k(\xi_j) + \left[q^{l,\text{avg}}_{k-\frac{1}{2}} - q^l_k(-1)\right]g'_L(\xi_i) + \left[q^{l,\text{avg}}_{k+\frac{1}{2}} - q^l_k(+1)\right]g'_R(\xi_i), \tag{45}$$

is shown. It follows the same steps as the divergence of the continuous flux at the k-th cell (see equation (26)) with the difference that, instead of the numerical upwind flux value recovered at the cell interfaces, the

average values between neighbors are used instead,

$$q^{l,\text{avg}}_{k-\frac{1}{2}} = \frac{q^l_{k-1}(+1) + q^l_k(-1)}{2} \quad \text{and} \quad q^{l,\text{avg}}_{k+\frac{1}{2}} = \frac{q^l_k(+1) + q^l_{k+1}(-1)}{2}. \tag{46}$$

Ultimately, the divergence of the SFS closure terms are added to the divergence of their respective fluxes, still performed with the Lax-Friedrichs procedure (26), to complete the system of equations and advance it in time. The step of averaging the SFS closure values at the cell interfaces is essential for numerical stability of the scheme because it is able to account for the instances when a discontinuity is traveling between cells. At the moment they are traveling between cells, the complete strength of the discontinuity is unknown in each separate cell and, therefore, the sharing of information at the interface aids the scheme in applying the necessary dissipation magnitude.

3.3 Inspection of the modulation transfer function curve

This subsection explains the details of an *a priori* analysis based on the exact solution to the Burgers' equation used to inform the design of the modulation transfer function curve (44).

An *a priori* analysis carried out in the context of large-eddy simulations exploits the solution coming from a direct numerical simulation (DNS) of the Navier-Stokes equations, which is taken as a reference in lieu of an unavailable analytical solution. The DNS solution is sharp-spectral-filtered ($\bar{\cdot}$) to compute the exact sub-filter scale (SFS) stresses, $\tau^{ij} = \overline{u^i u^j} - \overline{u}^i \overline{u}^j$ (Clark et al., 1979; Piomelli et al., 1988; Germano et al., 1991). These exact SFS stress values are compared against the output of SFS models driven by the exact filtered solution, $\overline{u}^i$, allowing to focus the analysis only on modeling errors.

The same procedure is used in the current manuscript with two important differences: (1) analytical solutions for 1D shock dominated flows are used as a reference solution instead of numerical DNS results; (2) the primary filter operation is sharp in the Legendre (rather than in the Fourier) spectral space. In one dimension the SFS stress tensor is reduced to the single component $\tau^{11} = \overline{u^1 u^1} - \overline{u}^1 \overline{u}^1$, which is the focus of the following *a priori* analysis.

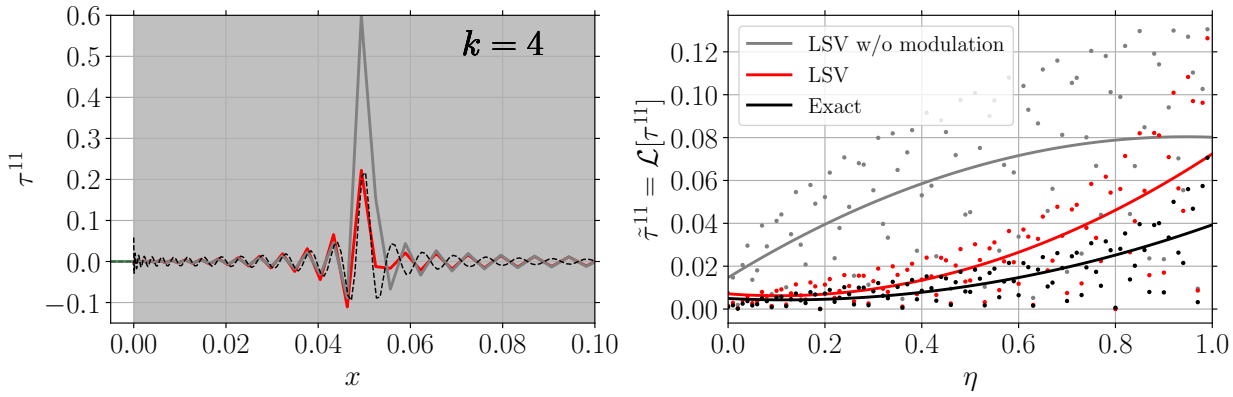

Figure 4: *A priori* analysis performed on the Burgers' equation with initial conditions given in equation (48) when the periodic domain $x^1 \in [-1, 1]$ is discretized with $K = 8$ cells and polynomial order of $N = 100$. Only the solution at time $t = 1.05$ and in the cell $k = 4$, which contains the shock, is shown. The spectrum of the τ^{11} stress is shown in the Legendre space, η, with colored dots. A fit is also shown with a solid line to show the effects of the LSV modulation, achieving a trend closer to the exact stresses.

The Burgers' test case, described in more detail in section 4.1, is used in the *a priori* analysis shown in figure 4 to showcase the spectral behavior of the exact SFS stress and the effect of the spectral modulation function (44). It can be observed that the magnitude of the exact $\tilde{\tau}^{11}$ – the Legendre transform of the exact τ^{11} term – generally increase with η with a convex shape, culminating with a peak near the cutoff, $\eta = 1$. A similar trend was also observed in theoretical studies of the spectral behavior of sub-filter scale turbulence by Kraichnan (1976) and Chollet and Lesieur (1981). It was observed that if the primary filter cutoff lies

in the inertial subrange, the resulting spectral decomposition of the eddy viscosity is not a flat function of the resolved wavenumber space: it exhibits, rather, a plateau at low wavenumbers and a sharp rise near the grid cutoff, referred to as the *plateau-cusp* behavior. A similar behavior was observed in the SFS stress term extracted from the Burgers' problem with a sharp spectral Fourier filter and such connection was used as an argument for building a unified shock capturing and turbulence model, as reported in Sousa and Scalo (2021).

Figure 4 also shows how spectral distribution of the SFS stresses predicted by the LSV model without the modulation operation (34) exhibits the wrong trend. The adoption of unmodulated SFS stresses would lead to increased dissipation values at the larger scales, i.e. lower Legendre modes, and could affect the accuracy of the resolved field. This effect is discussed further in 4.4. The results gathered from the LSV model with the modulation operation (34) active, follow much more closely the exact SFS stress component, removing unnecessary dissipation at the larger resolved scales.

4 Performance assessment of the LSV's closure

In this section, the proposed LSV's closure will be tested. First, the developed methodology is applied to the 1D Burgers' equation. Next, problems related to the inviscid compressible Navier-Stokes system of equations, i.e. the Euler equations, are tackled. Initially, the one-dimensional problems of the Riemann shock tube problem (Sod, 1978) and the Shu-Osher shock-entropy wave interaction (Shu and Osher, 1988) are addressed. Moving forward, a 2D inviscid strong shock-strong vortex interaction simulation is executed and, ultimately, a simulation of the 2D double Mach reflection problem is carried out. The aforementioned test cases are solved using a 3rd-order strong stability preserving (SSP) Runge-Kutta (Gottlieb et al., 2001) time integration method.

4.1 Burgers' Equation

The inviscid Burgers' equation is a nonlinear scalar conservation law that develops a discontinuity in a finite time and can be regarded as a simplified model of the nonlinearity present in the full Navier-Stokes system. Hereafter it is introduced alongside with its filtered version,

$$\frac{\partial u^1}{\partial t} + \frac{1}{2}\frac{\partial u^1 u^1}{\partial y^1} = 0, \quad \frac{\partial \overline{u}^1}{\partial t} + \frac{1}{2}\frac{\partial \overline{u}^1 \overline{u}^1}{\partial y^1} = -\frac{1}{2}\frac{\partial \tau^{11}}{\partial y^1}. \tag{47}$$

The same procedure used to achieve the filtered compressible Navier-Stokes equations (2) - (4) is repeated here to get the filtered Burgers' equation. Note that, in this simple equation, only one component (τ^{11}) of the SFS fluxes is present. Its simplicity, though, allows for an analytical solution through the method of characteristics given a certain initial condition and, therefore, allows for a performance assessment of the LSV closure model in both *a priori* and *a posteriori* analysis. The following initial condition,

$$u^1(x, t = 0) = 1 + \frac{1}{2}\sin(\pi x), \tag{48}$$

in a periodic domain $x \in [-1, 1]$ is chosen as the basis of the numerical study. It represents a traveling nonlinear pulse which steepens until a discontinuity is formed.

The LSV closure model is used to simulate the evolution of the initial condition, equation (48), until $t = 1$. The results in figure 5 gather the combinations of simulations with $K = 10,\ 20$ and 40 cells with polynomial orders of $N = 4,\ 8$ and 12. They show that both the refinement in the number of cells and the expansion in polynomial order are capable of increasing the accuracy of the final solution and concentrating the numerical errors near the region of discontinuity. This is an interesting result that showcases the capability of the model to perform internal cell shock capturing. As previously mentioned, the Gibbs oscillations near the discontinuities are a consequence of attempting to diminish the dissipation on the resolved spectrum of the solution.

Additionally, the current method is shown to be robust at even very high-order of polynomial reconstruction. Inspired by Asthana et al. (2015)'s result of a steady Burger's equation solution being captured by a 119-th order polynomial reconstruction within the center cell of a three-element configuration, figure 6 shows

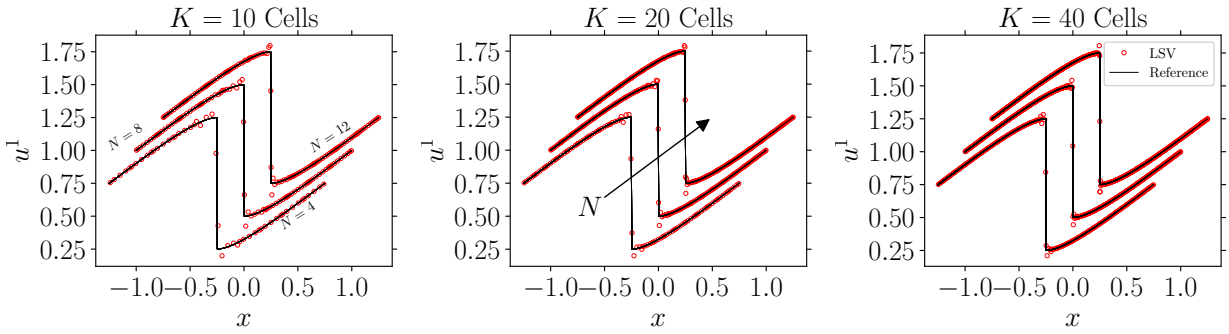

Figure 5: High-order flux reconstruction numerical solution of the Burger's equation using the LSV closure. The domain is discretized with a combination of $K = [10, 20, 40]$ cells and $N = [4, 8, 12]$ polynomial orders and the initial condition given in equation (48) is solved up to $t = 1$ in a periodic domain $x^1 \in [-1, 1]$. The analytical solution is shown in fine solid black lines and the numerical results at the solution points are show in red circular markers.

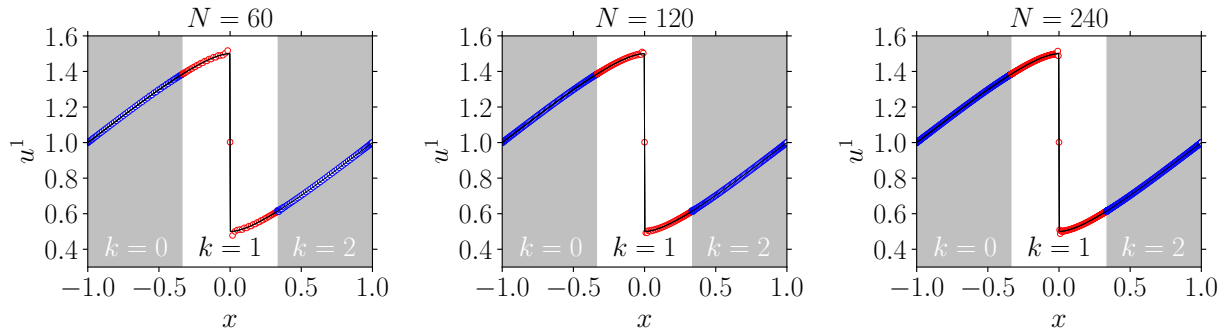

Figure 6: Flux reconstruction numerical solution of the Burger's equation using the LSV closure for very high-order polynomials. In this case $K = 3$ cells are used to discretize the domain and, in turn, each cell is solved with polynomial orders of $N = [60, 120, 240]$. The initial condition given in equation (48) is solved up to $t = 1$ in a periodic domain $x^1 \in [-1, 1]$. The analytical solution is shown in fine solid black lines and the numerical results at the solution points are show in alternating red or blue circular markers. Regions corresponding to different cells are periodically shaded.

results for an advecting nonlinear pulse solved with $K = 3$ and $N = 60, 120$ and 240. This shows that, not only the current method is capable of performing a very high-order solution of a discontinuity within a cell, but also to allow the discontinuity to move seamlessly from a neighboring cell to another.

4.2 Sod shock tube

Moving forward, the focus is changed from a scalar nonlinear conservation law to the inviscid Navier-Stokes system of equations in one dimension, i.e. the Euler equations. If the aforementioned system of equations is initialized with the following initial conditions in density, velocity and pressure,

$$[\rho, u^1, p](x, 0) = \begin{cases} [1, 0, 1], & \text{if } x < 0.0 \\ [0.125, 0, 0.1], & \text{otherwise,} \end{cases} \tag{49}$$

for $x^1 \in [-1, 1]$, then a shockwave propagating to the right develops. An exact solution can be found for this setting, known as the Sod shock tube problem (Sod, 1978), and it consists of 4 constant density states separated by a shock, a contact discontinuity and a rarefaction wave.

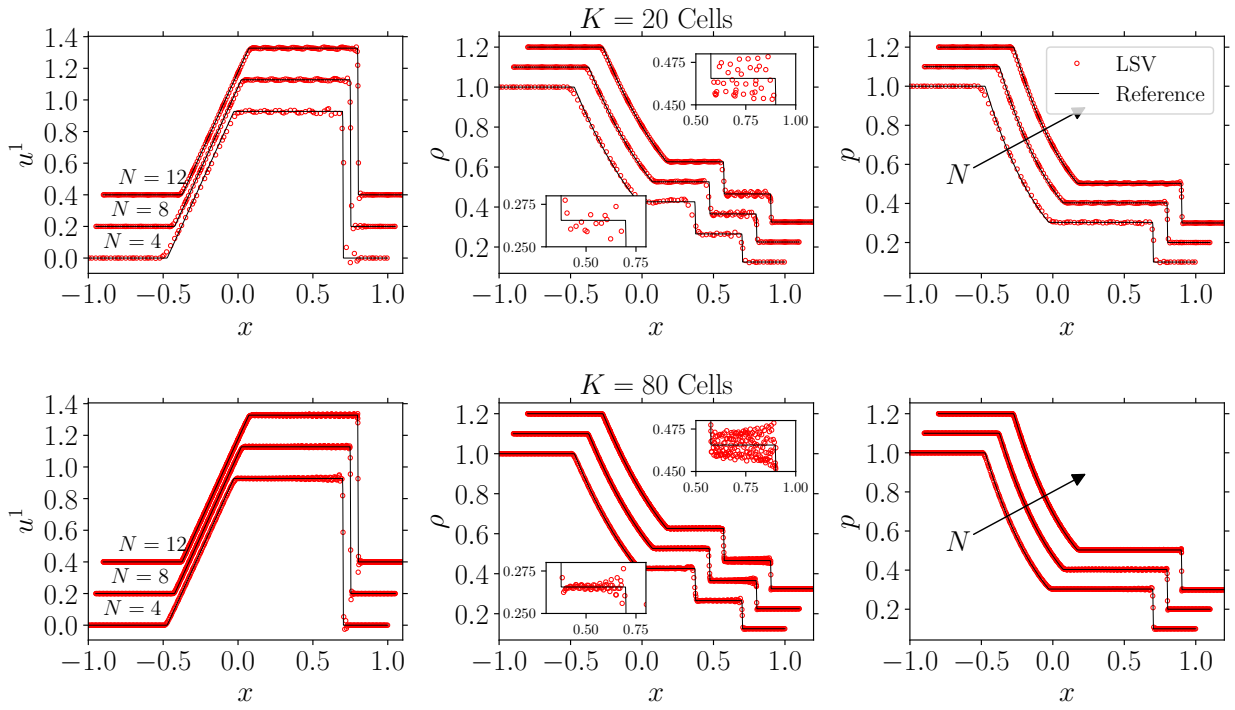

Figure 7: High-order flux reconstruction numerical solution of the Sod shock tube problem (Sod, 1978) using the LSV closure. The domain is discretized with a combination of $K = [20, 80]$ cells and $N = [4, 8, 12]$ polynomial orders and the initial condition is solved up to $t = 0.4$. The analytical solution is shown in fine solid black lines and the numerical results at the solution points are show in red circular markers.

In progression, the Sod shock tube problem (Sod, 1978) is simulated up to $t = 0.4$. The computational domain is discretized with combinations of $K = [20, 80]$ cells and polynomials of order $N = [4, 8, 12]$. Figure 7 gathers the results of this numerical experiment. It can be observed that a refinement in either the total number of cells or the order of the polynomial reconstruction within each cell leads to a sharper gradient capturing near discontinuities as well all as increased accuracy on the remaining of the computational domain. Throughout the domain, but mainly in the region between the contact discontinuity and the shock in the density field, it is possible to observe some high wavenumber spurious oscillations for all the number of cells and polynomial orders tested, also present in simulations performed by Haga and Kawai (2019). These oscillations are low in amplitude, at most $\delta\rho = 0.03$, and are more pronounced at higher-orders. Their amplitude decreases with cell number refinement but superior levels of refinement are needed if higher order polynomials are used. Another strategy is to further increase the dissipation levels of the resolved spectrum but this may lead to unnecessary damping of the physically relevant oscillations in the resolved field that occur near the resolution limit. An analysis of such a scenario is provided in 4.4.

Once more, the robustness of the current method is shown, in figure 8, by simulating a Sod shock tube problem, a nonlinear coupled system, using polynomials orders of $N = [90, 120, 150]$ with $K = 3$ cells. This is an extension of what was previously published by Asthana et al. (2015), who limited their very high-order simulations to the Burgers' equation. Moreover, although the simulation is performed at $N \geqslant 90$, the presence of spurious oscillations is greatly attenuated. This is a consequence of the domain being discretized with only three separate cells. Because of that, at least a third of the domain, i.e. the cell in which the discontinuity is present, is subjected to the dissipation added by the LSV closure. This can be desirable if no physical small scales are present in the simulation but it can also lead to a decrease in resolution power if that is not the case. Despite a decrease in the presence of low-amplitude high-frequency oscillations, a small kink of amplitude $\delta\rho \approx 0.01$ is observed in the density field between the contact discontinuity and the main shock. This is a consequence of allowing small overshoots to occur in exchange for the ability to retain high

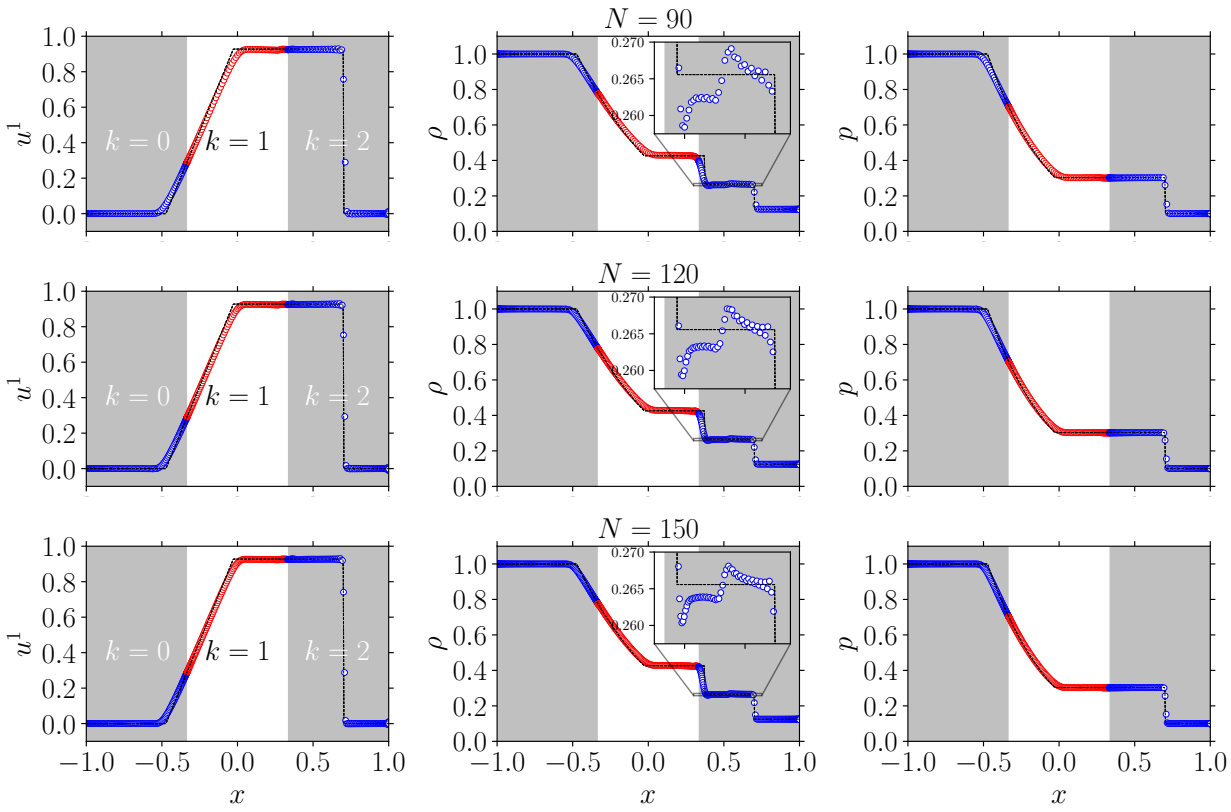

Figure 8: Flux reconstruction numerical solution of the Sod shock tube problem (Sod, 1978) using the LSV closure for very high-order polynomials. In this case $K = 3$ cells are used to discretize the domain and, in turn, each cell is solved with polynomial orders of $N = [90, 120, 150]$. The analytical solution is shown in fine solid black lines and the numerical results at the solution points are show in alternating red or blue circular markers. Regions corresponding to different cells are periodically shaded.

wavenumber information. Ultimately, this is not a concern since the amplitude of the kink decreases with an increase in the polynomial order, as the method converges to the exact solution.

4.3 Shu-Osher shock-entropy wave interaction

Moving forward, focus is given to the shock-entropy wave interaction introduced by Shu and Osher (1988). The setup comprises a shock wave propagating into a resting fluid where small amplitude density perturbations are present. Upon interaction with the shock, two phenomena occur: the initially smooth density perturbations steepen and form weak shocks; small-scale acoustic waves that trail the main shock are generated. This numerical test case is challenging because sufficient dissipation is needed to capture the shock discontinuity but, at the same time, the overall dissipation must be limited to prevent a spurious attenuation of the trailing waves.

The Shu-Osher shock-entropy wave interaction problem is defined by the following initial conditions in the domain $x \in [-1, 1]$,

$$[\rho, u, p](x, 0) = \begin{cases} [3.857143, 2.629369, 10.333333], & \text{if } x < -0.8 \\ [1.0 + 0.2\sin(25x), 0.0, 1.0], & \text{otherwise,} \end{cases} \tag{50}$$

which are advanced up until $t = 0.36$. Figure 9 gathers the results for the density field when the LSV closure is used and the computational domain is discretized with a combination of $K = [20, 40, 80]$ cells and a polynomial order equivalent to $N = [4, 8]$. The outcome of such simulations are compared against a finely

discretized run with 500 cells and order 3, taken here as a direct numerical simulation of the Shu-Osher problem. It can be observed that the refinement in either direction regarding total number of cells or inner cell polynomial order lead to better results in respect to sharper gradients near discontinuities and smaller attenuation of the trailing wave packet. A subset of these results can be compared against similar simulations performed by Haga and Kawai (2019), where 400 degrees of freedom (DOF) where used. The case where $K = 40$, $N = 8$ and $K = 80$, $N = 4$ have 360 and 400 DOFs respectively and both show qualitatively similar results when compared to Haga and Kawai (2019)'s. Despite the similarity in resolution capacity, the current method is able to surpass the 4-th order polynomial order limitation existent in the aforementioned method.

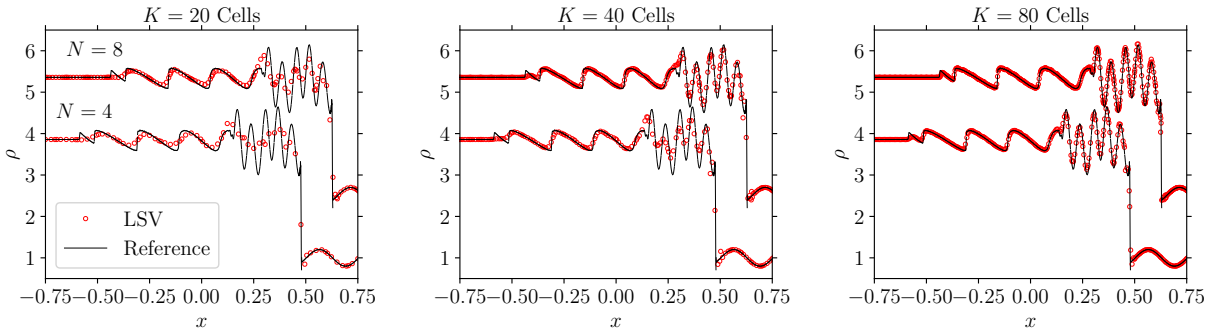

Figure 9: High-order flux reconstruction numerical solution of the Shu-Osher shock-entropy wave interaction (Shu and Osher, 1988) using the LSV closure. The domain is discretized with a combination of $K = [20, 40, 80]$ cells and $N = [4, 8]$ polynomial orders and the initial condition is solved up to $t = 0.36$. Numerical results at the solution points are show in red circular markers and are compared against a DNS performed with 500 cells and order 3, shown in fine solid black lines.

The last item to be addressed in the current subsection is a comparison of results obtained by the current method and the one published by Asthana et al. (2015). For that, a slight modification to the Shu-Osher problem must be made to allow for direct comparison. Asthana et al. (2015) performed a change of reference and simulated a stationary shock towards which the initially sinusoidal entropy waves traveled and interacted. Additionally, higher frequency entropy waves are used in the initial condition. Such version of the problem is defined for $x \in [-1, 1]$ as

$$[\rho, u, p](x, 0) = \begin{cases} [3.857143, -0.920279, 10.333333], & \text{if } x < 0.0 \\ [1.0 + 0.2\sin(50x), -3.549648, 1.0], & \text{otherwise.} \end{cases} \tag{51}$$

The comparison between the current method based on the LSV closure and Asthana et al. (2015)'s results is displayed in figure 10. The present implementation outperforms the previously published method with respect to the capacity of accurately solving the small scales that occur in the wavepacket trailing the main shock discontinuity. This conclusion is drawn because, even though the same polynomial order of $N = 8$ was used for both methods, if the same number of cells of $K = 56$ is used, the LSV based simulation is able to recover most of the rear shock dynamics and, in turn, Asthana et al. (2015)'s method dissipates much of the high wavenumber oscillations. In fact, the previously published method needs approximately 8 times as much cells, $K = 448$, to retain a similar accuracy in the post shock region. It is possible that the parameters for Asthana et al. (2015)'s method might be able to be better adjusted and optimized to resolve the flow physical small-scale content. That being said, the version of the model reported in the literature has shown difficulties in resolving such waves.

4.4 Effects of the spectral modulation operation on the solution of 1D shock-dominated problems

In this subsection, the Sod shock tube (Sod, 1978) and the shock-entropy wave interaction introduced by Shu and Osher (1988) are simulated using the LSV closure with and without the spectral modulation operation

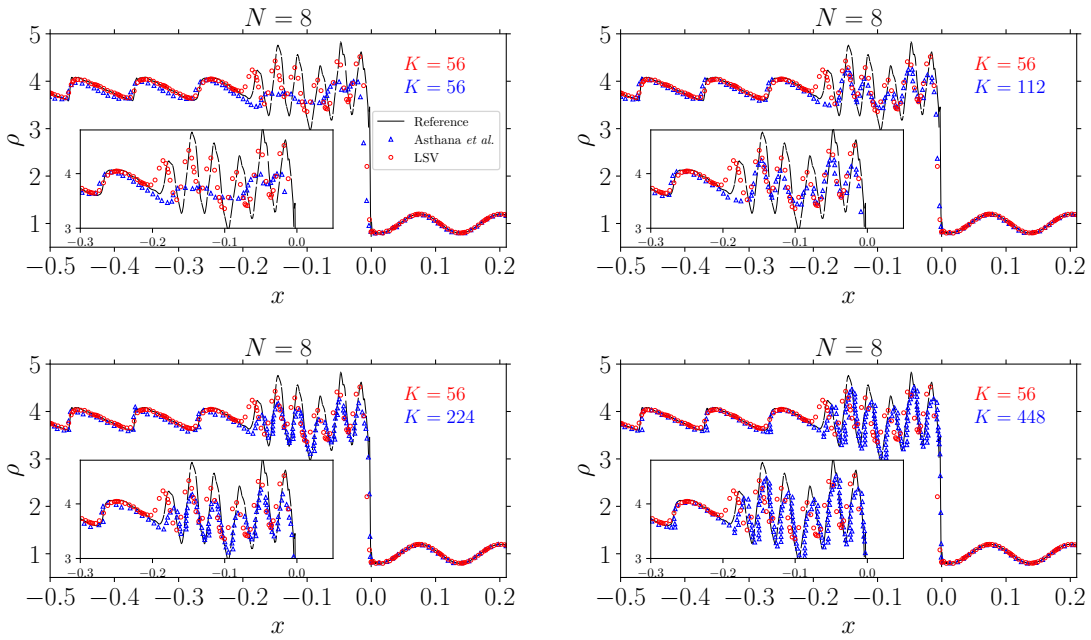

Figure 10: High-order flux reconstruction numerical solution of the Shu-Osher Shock-Entropy Wave Interaction (Shu and Osher, 1988) using the LSV closure is compared against Asthana et al. (2015)'s method. The domain is discretized with a polynomial order of $N = 8$. The results simulated with LSV using $K = 56$ cells, shown in red circles, are compared against digitized results published by Asthana et al. (2015) for $K = [56, 112, 224, 448]$, shown in blue triangles. A reference solution is obtained by solving the initial condition up to $t = 0.2$ with 500 cells using order 3, shown in fine dashed lines.

(34) to showcase the effects that such a procedure causes to the final solution.

Figure 11 shows that the increase in dissipation magnitude across all the resolved wavenumbers associated with skipping the spectral modulation operation (see figure 4) is able to decrease the amplitude of the spurious oscillations present specially in the density field at the region between the main shock and the contact discontinuity. This decrease occurs for all combinations of number of cells and polynomial orders considered but its effectiveness is particularly observed at $K = 80$ cells and $N = 12$ order. At such a resolution, the simulation without the modulation operation is capable of decreasing the observed high-frequency oscillations' magnitude by a factor of 3.

However, the increase in the added dissipation across the resolved spectrum can also lead to dissipation of physical small-scale oscillations such as the ones present in the Shu-Osher problem. Figure 12 shows that the simulations performed without the spectral modulation operation are consistently further from the reference solution in comparison with the default LSV closure setup for all grid arrangements considered. For example, at the $K = 40$ and $N = 8$ resolution, the full LSV results for the acoustic waves trailing the main shock are fairly close to the grid resolved simulation while the ones achieved by skipping the spectral modulation operation display significantly lower magnitude.

Ultimately, the choice was made to accurately retain as much spectral information as possible in the resolved solution for a given grid resolution in the LSV methodology, even though such choice leads the occurrence of low-amplitude high-frequency oscillations in the solution.

4.5 Inviscid strong shock-strong vortex interaction

A stationary shock supported by a supersonic inflow velocity of $V_0 = 1.5\sqrt{\gamma p_0/\rho_0}$ is initialized at $x_s/L = 1/2$ inside a computational domain $\Omega = [0, 2L] \times [0, L]$. A compressible zero-circulation vortex is initialized upstream of the shock at $(x_v/L, y_v/L) = (1/4, 1/2)$ with an inner core radius equal to $a/L = 0.075$ and an external radius $b/L = 0.175$. This can be translated as $\mathbf{u} = u_\theta(r)\hat{\mathbf{e}}_\theta + V_0\hat{\mathbf{e}}_x$, where r is the radial distance

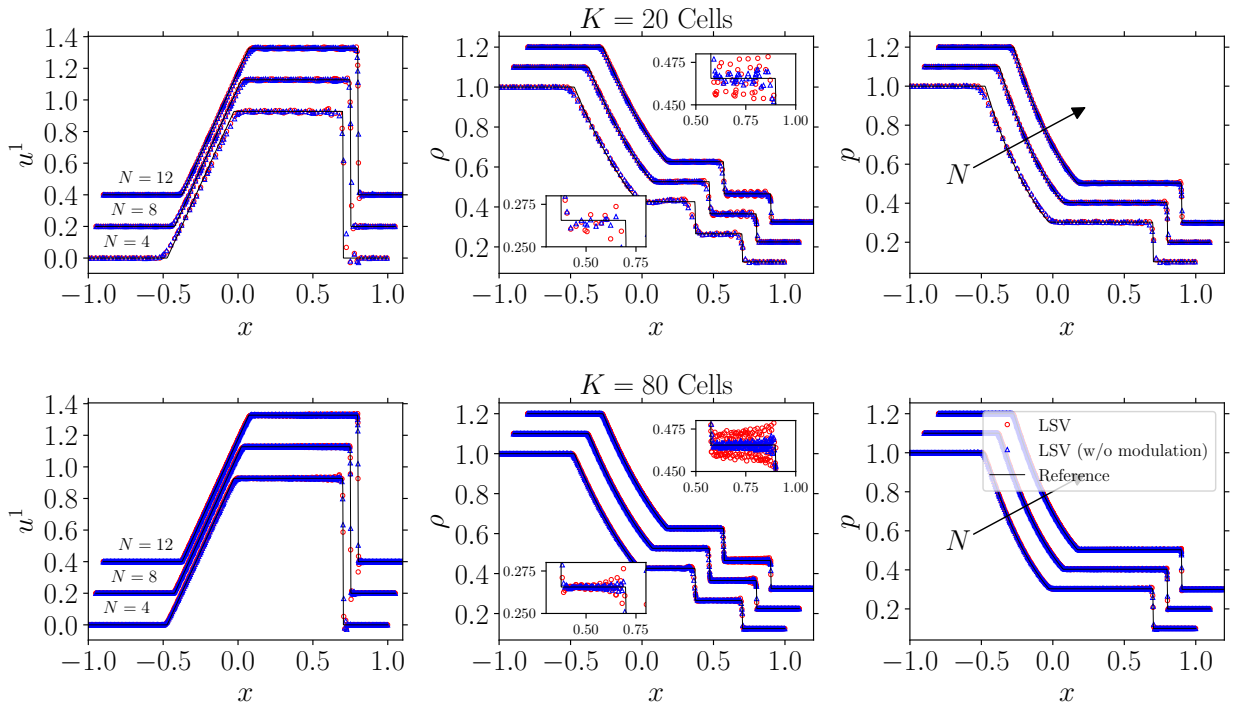

Figure 11: High-order flux reconstruction numerical solution of the Sod shock tube problem (Sod, 1978) using the LSV closure with and without the application of the spectral modulation procedure (34). The domain is discretized with a combination of $K = [20, 80]$ cells and $N = [4, 8, 12]$ polynomial orders and the initial condition is solved up to $t = 0.4$.

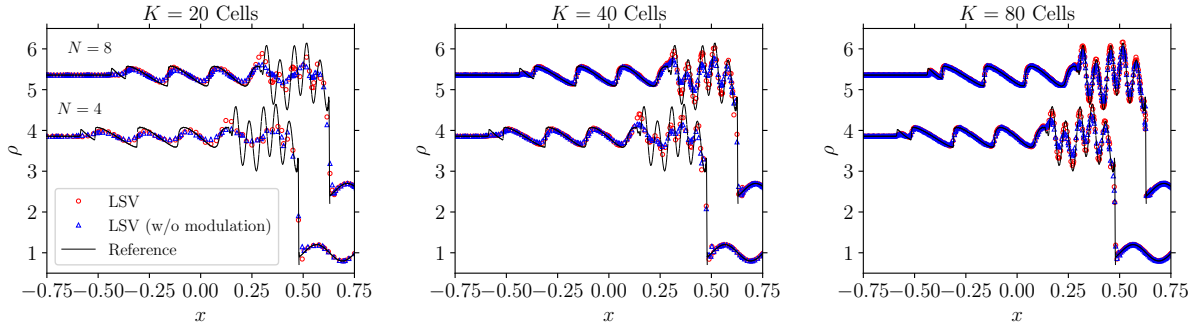

Figure 12: High-order flux reconstruction numerical solution of the Shu-Osher shock-entropy wave interaction (Shu and Osher, 1988) using the LSV closure with and without the application of the spectral modulation procedure (34). The domain is discretized with a combination of $K = [20, 40, 80]$ cells and $N = [4, 8]$ polynomial orders and the initial condition is solved up to $t = 0.36$. Numerical results at the solution points are compared against a DNS performed with 500 cells and order 3, shown in fine solid black lines.

from the center of the vortex and

$$\frac{u_\theta(r)}{u_\theta(a)} = \begin{cases} \frac{r}{a}, & \text{if } r \leqslant a \\ \frac{\eta}{2}\left(\frac{r}{b} - \frac{b}{r}\right), & \text{if } a < r \leqslant b \\ 0, & \text{otherwise,} \end{cases} \tag{52}$$

where $\eta = 2(b/a)/[1-(b/a)^2]$ and the maximum tangential velocity is set to $u_\theta(a) = 0.9V_0$. Following the pressure field is initialized so that its gradient balances the centripetal force and the following system of equations is solved based on the ideal gas relation and isentropic compression,

$$\frac{\partial P}{\partial r} = \rho\frac{u_\theta^2(r)}{r}, \quad P = \rho RT, \quad \frac{P}{P_0} = \left(\frac{\rho}{\rho_0}\right)^\gamma. \tag{53}$$

Ellzey et al. (1995) first employed such a setup to examine the acoustic field generated by the shock-vortex interaction. Following publications by Rault et al. (2003) and by Tonicello et al. (2020) also used the same arrangement to analyze the driving mechanisms for the production of vorticity due to the interaction with shocks and to investigate shock capturing techniques in high-order methods focused on their influence on the entropy field and its non monotonic profile across a shock, respectively.

Previous literature reports that a shock/vortex interaction leads to the compression of an initial circular vortex into an elliptical shape with the ultimate distortion being dependent on shock strength (Dosanjh and Weeks, 1965; Grasso and Pirozzoli, 2000). Additionally, for the strong shock, $M_s = 1.5$, and strong vortex, $M_v = 0.9$, case considered, highly resolved simulations show a S-shaped deformation of the shock front upon interaction and, ultimately, a symmetry break which culminates with the formation of two new counter-clockwise rotating vortices, being the top one ahead of its bottom counterpart (Rault et al., 2003; Tonicello et al., 2020; Sousa and Scalo, 2021). A grid-refined LSV simulation (figure 13) displays the aforementioned phenomena as well as the formation of reflected shocks and a Mach stem as discussed by Ellzey et al. (1995), seen around $tV_0/L \approx 0.35$. These results, gathered from a run with approximately 2.1 million degrees-of-freedom (DOF), are also used as reference to compare the resolution power of different grid refinement levels hereafter.

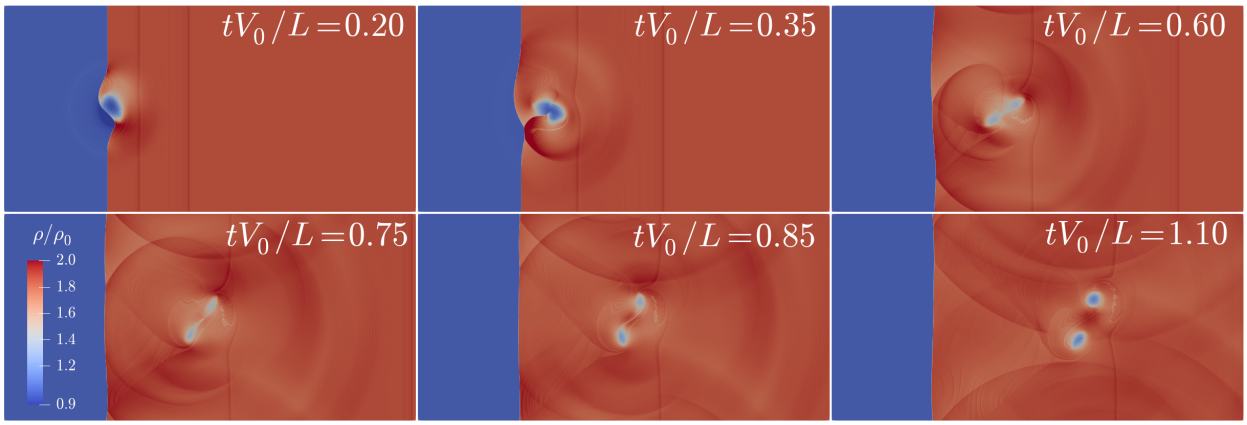

Figure 13: LSV simulation of an inviscid strong shock-strong vortex interaction performed with $N = 7$ polynomial order in both directions and $K_x \times K_y = [256 \times 128]$ cells, a total of 2097152 DOF. Six different time instants are shown to illustrate the system's development.

A grid sensitivity analysis is performed for the LSV simulations of such shock/vortex interaction and the results are collected in figure **??**. Simulations with different degrees-of-freedom (DOF) were performed and their results are compared at time $tV_0/L = 1.10$, when vortex separation is expected. The pressure field at the center of the domain is extracted for each simulation at different time instants and compared against a LSV reference solution performed with approximately 2.1 million DOF (figure 13). Initially, it can be inferred that an increase in the number of DOF is directly correlated with an increase accuracy independently of how the refinement was achieved – whether with an increase in the number of cells or an increase in the polynomial order used within each cell. Ultimately, at the finest refinement level in this analysis, the solution for all polynomial orders contemplated converged to the reference result.

A more thorough analysis shows that matching between the coarse solutions and the reference result for the same DOF first increases and then decays with increasing polynomial order. It can be observed that intermediate polynomial order of $N = 7$ is closer to the reference solution for a given total DOF level in

comparison with the others, followed by $N = 3$ and $N = 15$. These results happen due to the larger cell sizes, associated with higher-order simulations in constant DOF settings, spreading the added dissipation throughout a larger area around the main shock discontinuity. Ultimately, though, the results gathered from the simulations performed with approximately 130000 DOF follow closely the ones from the converged reference solution, 16 times finer.

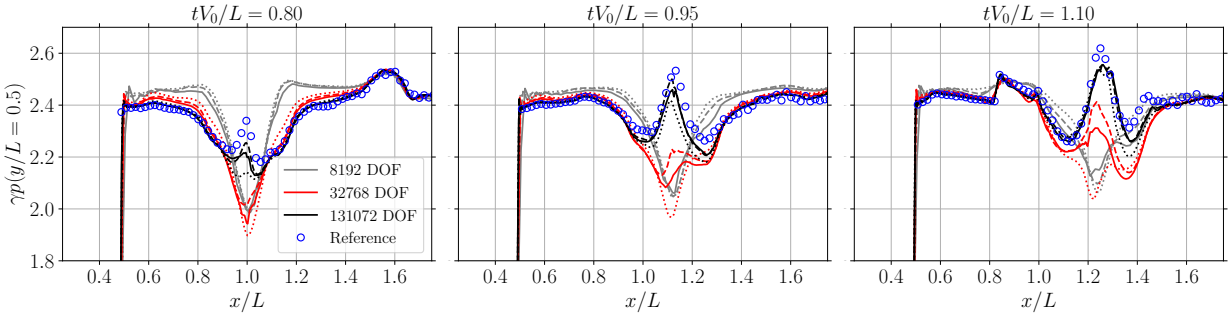

Figure 14: Pressure field at the center of the domain resulting from a strong shock-strong vortex interaction at various instants in time. Different grid resolution levels, measured by the total number of degrees-of-freedom (DOF), are compared against a reference solution (figure 13). The different polynomial orders are distinguished by their particular line styles: low. $N = 3$, is shown in solid lines (——), intermediate, $N = 7$, in dashed lines (- - - -) and high, $N = 15$, in dotted lines (·····).

4.6 Double Mach Reflection

The double Mach reflection problem of Woodward and Colella (1984) is a challenging test case for the 2D unsteady Euler equations. A Mach 10 shock is introduced in the computational domain $\Omega = [0, 4] \times [0, 1]$ at a 60-degree angle with respect to the lower boundary. The left and right states are defined as

$$\rho = \begin{cases} \rho_l = \frac{(\gamma+1)M^2}{2+(\gamma-1)M^2}, \\ \rho_r = 1, \end{cases} \qquad u = \begin{cases} u_l = V_l \cos(30), \\ u_r = 0, \end{cases} \tag{54}$$

$$v = \begin{cases} v_l = -V_l \sin(30), \\ v_r = 0, \end{cases} \qquad p = \begin{cases} p_l = \frac{2\gamma M^2-(\gamma-1)}{\gamma(\gamma+1)}, \\ p_r = 1/\gamma, \end{cases} \tag{55}$$

where $V_l = M - a_r\sqrt{\frac{(\gamma-1)M^2+2}{2\gamma M^2-(\gamma-1)}}$, $a_r = \sqrt{\gamma\frac{p_r}{\rho_r}}$ is the speed of sound at the right state. In the current simulations the value $\gamma = 1.4$ was considered. At time $t = 0$, the shock front touches the bottom boundary at $x = 1/6$ and is kept attached by assigning the left state values to the region where $x < 1/6$. For $x \in [1/6, 4]$, a reflecting wall boundary condition is applied at the bottom wall. At the top wall, a time dependent boundary condition that follows the shock front at $x_s = 1/6 + \frac{1+2Mt}{\sqrt{3}}$ is used to apply the correct left or right states. Ultimately, inflow and outflow conditions are assigned to the left and right boundaries, respectively. Such a setup was used by Kuzmin (2014) to study slope limiting in discontinuous Galerkin methods and by Asthana et al. (2015) to analyze the Fourier-spectral filtering method in flux reconstruction settings.

Due to the substantial pressure jump imposed by the Mach 10 shock, in the order of 100, the positivity of the pressure field was difficult to maintain for a high-order discretization. It is shown in Zhang (2017) that the use of SSP Runge-Kutta time advancement together with a suitable positivity preserving flux is able to ensure a *weak positivity* property for the compressible Navier-Stokes equations. That is, given a sufficiently small enough time step, the positivity of the average of the cell values can be assured. Furthermore, if one analyzes the filtered compressible Navier-Stokes system of equations, one can observe that it has the same structure as the original equations with the addition of extra dissipative terms that come from the sub-filter scale (SFS) closure. Since the SFS terms have the same mathematical structure as the original stress tensor and heat flux vector, it is possible to construct a positivity-preserving flux that accounts for the SFS contributions.

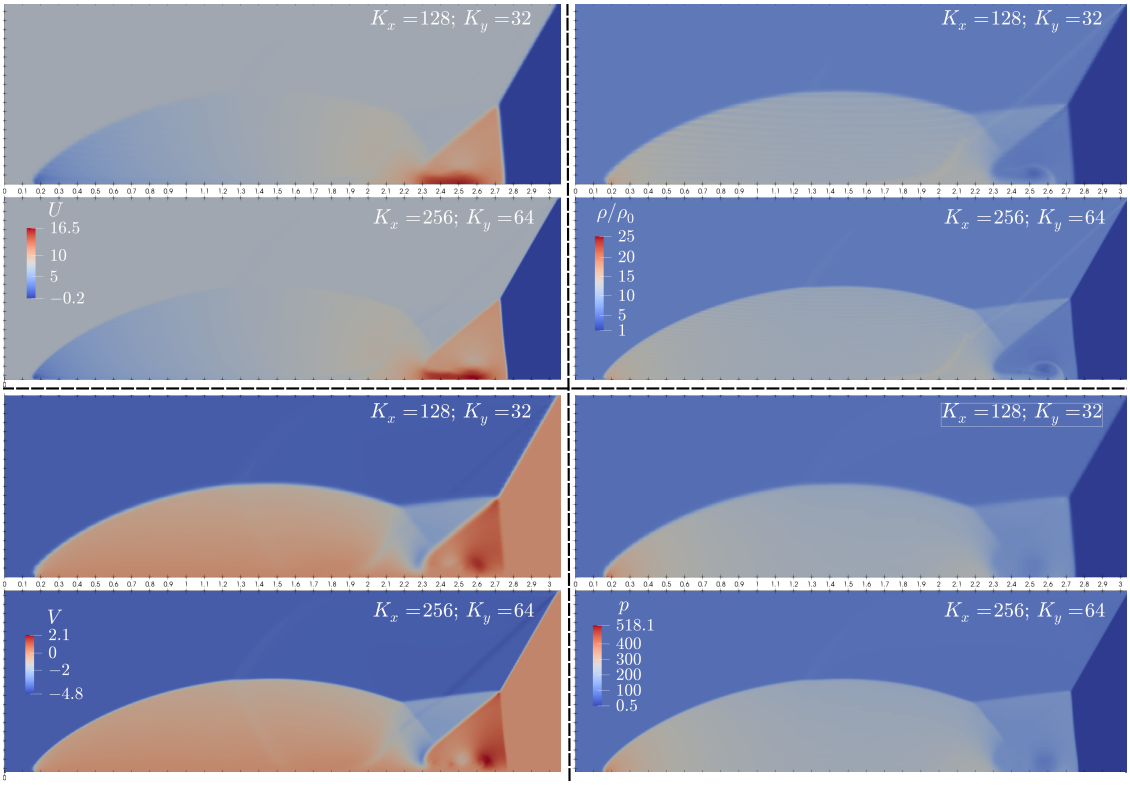

Figure 15: Simulations of the reflection of a Mach 10 shock performed with $N = 4$ polynomial order in both directions and $K_x \times K_y = [128 \times 32, 256 \times 64]$ cells. Results for the pressure, density and velocity fields are shown at time $t = 0.2$.

This, though, does not ensure pointwise positivity and, in Zhang (2017), a scaling limiter that suppresses the solution without changing the average value is used to achieve the global positivity property. Although this procedure is, in theory, compatible with the current LSV flux reconstruction-based implementation because it allows discontinuous solutions at cell interfaces, this step was not applied in the current work. Additionally, although it would be interesting to test the use of the developed positivity-preserving flux for the compressible Navier-Stokes equations (Zhang, 2017) in the current setup, the original choice of adopting the Lax-Friedrichs flux was retained and a study on the different numerical fluxes is left for future work. Ultimately, the increase in upwind degree that would be introduced by the novel flux formulation was substituted by a higher dissipation magnitude in this particular test case.

To ensure numerical stability in the current double Mach reflection 4-th order runs, it was necessary to increase the magnitude of the components of the dissipation tensor, $\mathcal{D}^{ij}$ (36), by a factor of 3. Asthana et al. (2015) also reports the necessity of intensifying the added dissipation to simulate the double mach reflection stably, what was done by decreasing the threshold for the discontinuity sensor. A point for further investigation should be the effect of considering the Reynolds-based filtered equations, which would lead to different subfilter flux terms that include a SFS density flux term and could possibly lead to implementations with higher numerical stability.

Figure 15 gathers the results for the pressure, density and velocity fields for the double Mach reflection problem at $t = 0.2$, when simulations are performed with a 4-th order polynomial and $K_x \times K_y = [128 \times 32, 256 \times 64]$ cells. It can be observed that a high speed jet is formed at the center of the domain near the shock front and, in turn, the induced shear causes the formation of a vortex, most evidenced in the density field. Additionally, the grid refinement leads to sharper gradients at the shock boundaries, higher resolution of small scales in the vortex region, and decreased spurious density oscillations in the density field. The finest simulation here uses 409,600 degrees-of-freedom, about 2.5 times lower than Asthana et al. (2015) for qualitatively similar results. Moreover, the finest simulation carried in the current work recovers considerably

more flow dynamic details when compared to the finest resolution simulation performed by Kuzmin (2014), which had 65,536 elements with 2nd order, equivalent to 589,824 DOFs.

5 Conclusion

A novel technique for discontinuity capturing for high-order Flux Reconstruction (FR) schemes named the Legendre Spectral Viscosity model (LSV), was introduced. It relies on solving the large scales present in shock-dominated flows while dissipating the small scales. This is achieved by solving for filtered versions of the original nonlinear conservation equations and modeling the energy flux to subfilter scales as a dissipative term. Ultimately, it is a generalization of the mathematical framework used in Large Eddy Simulations (LES) to shock-dominated problems.

The novelty of the LSV method relies on exploiting the connection between FR implementation and the Legendre polynomials to project the solution within each cell onto the naturally occurring Legendre set of hierarchical basis functions. This step is performed to both estimate the magnitude of the needed dissipative term as well as modulate the dissipation behavior at different scales. In consequence, the LSV method is able to introduce a spectrally concentrated at small scales dissipative term that is active only in cells where nonlinear dynamics are important.

The LSV closure was successfully tested in one- and two-dimensional shock-dominated problems, being able to outperform consistently results shown in Asthana et al. (2015), by requiring less degrees of freedom to achieve the same level of accuracy. Additionally, although qualitatively similar results are recovered when compared against previous 1D shock/entropy wave interaction results by Haga and Kawai (2019), the current method is able to surpass the 4-th order limitation existent in the approach discussed in the aforementioned publication.

The results gathered here show the high performance of the LSV closure model in discontinuity capturing in high-order flux reconstruction settings. In the future, it is proposed to extend the methodology to model turbulence and shocks concomitantly, in the example of Sousa and Scalo (2022b), who showed that a similar setup for high-order finite difference solvers can perform both tasks at the same time.

References

K. Asthana, M. R. López-Morales, and A. Jameson. Non-linear stabilization of high-order flux reconstruction schemes via Fourier-spectral filtering. *Journal of Computational Physics*, 303:269–294, 2015.

F. Bassi and S. Rebay. A high-order accurate discontinuous finite element method for the numerical solution of the compressible Navier-Stokes equations. *J. Comput. Phys.*, 131(2):267–279, 1997.

P. Batten, N. Clarke, C. Lambert, and D. M. Causon. On the choice of wavespeeds for the HLLC Riemann solver. *SIAM Journal on Scientific Computing*, 18(6):1553–1570, 1997.

J. Chollet and M. Lesieur. Parameterization of small scales of three-dimensional isotropic turbulence utilizing spectral closures. *J. Atmo. Sci.*, 38(12):2747–2757, 1981.

R. A. Clark, J. H. Ferziger, and W. C. Reynolds. Evaluation of subgrid-scale models using an accurately simulated turbulent flow. *Journal of fluid mechanics*, 91(1):1–16, 1979.

B. Cockburn and C. W. Shu. TVB Runge-Kutta local projection discontinuous Galerkin finite element method for conservation laws. II. General framework. *Math. Comp.*, 52(186): 411–411, May 1989. ISSN 0025-5718. doi: 10.1090/S0025-5718-1989-0983311-4. URL `http://www.ams.org/jourcgi/jour-getitem?pii=S0025-5718-1989-0983311-4`.

A. W. Cook. Artificial Fluid Properties for Large-Eddy Simulation of Compressible Turbulent Mixing. *Physics of fluids*, 19(5):055103, 2007.

D. S. Dosanjh and T. M. Weeks. Interaction of a starting vortex as well as a vortex street with a traveling shock wave. *AIAA journal*, 3(2):216–223, 1965.

J. L. Ellzey, M. R. Henneke, J. M. Picone, and E. S. Oran. The interaction of a shock with a vortex: shock distortion and the production of acoustic waves. *Physics of Fluids*, 7(1):172–184, 1995.

U. Frisch. *Turbulence: the legacy of A. N. Kolmogorov*. Cambridge University Press, Cambridge, 1995.

M. Germano, U. Piomelli, P. Moin, and W. Cabot. A dynamic subgrid-scale eddy viscosity model. *Phys. Fluids A*, 3:1760–1765, 1991.

S. Godunov and I. Bohachevsky. Finite difference method for numerical computation of discontinuous solutions of the equations of fluid dynamics. *Matematičeskij sbornik*, 47(3):271–306, 1959.

D. Gottlieb and C.-W. Shu. On the Gibbs phenomenon and its resolution. *SIAM review*, 39(4):644–668, 1997.

S. Gottlieb, C. Shu, and E. Tadmor. Strong stability-preserving high-order time discretization methods. *SIAMR*, 43(1):89–112, 2001.

F. Grasso and S. Pirozzoli. Shock-wave–vortex interactions: shock and vortex deformations, and sound production. *Theoretical and Computational Fluid Dynamics*, 13(6):421–456, 2000.

P. Gupta and C. Scalo. Spectral energy cascade and decay in nonlinear acoustic waves. *Phys. Rev. E*, 98:033117, Sep 2018. doi: 10.1103/PhysRevE.98.033117. URL `https://link.aps.org/doi/10.1103/PhysRevE.98.033117`.

T. Haga and S. Kawai. On a robust and accurate localized artificial diffusivity scheme for the high-order flux-reconstruction method. *Journal of Computational Physics*, 376:534–563, 2019.

A. Harten, P. D. Lax, and B. v. Leer. On upstream differencing and godunov-type schemes for hyperbolic conservation laws. *SIAM review*, 25(1):35–61, 1983.

H. Huynh. A Flux Reconstruction approach to high-order schemes including discontinuous Galerkin methods. *AIAA Paper*, 2007-4079:1–42, 2007. 18th AIAA Computational Fluid Dynamics Conference, Miami, FL, Jun. 25–28, 2007.

A. Jameson, P. E. Vincent, and P. Castonguay. On the non-linear stability of flux reconstruction schemes. *Journal of Scientific Computing*, 50(2):434–445, 2012.

S. A. Jordan. A large-eddy simulation methodology in generalized curvilinear coordinates. *Journal of Computational Physics*, 148(2):322–340, 1999.

G. Karniadakis and S. Sherwin. *Spectral/hp element methods for computational fluid dynamics*. Oxford University Press, 2013.

S. Kawai and S. K. Lele. Localized Artificial Diffusivity Scheme for Discontinuity Capturing on Curvilinear Meshes. *Journal of Computational Physics*, 227(22):9498–9526, 2008.

S. Kawai, S. K. Shankar, and S. K. Lele. Assessment of localized artificial diffusivity scheme for large-eddy simulation of compressible turbulent flows. *Journal of Computational Physics*, 229(5):1739–1762, 2010.

D. A. Kopriva and J. H. Kolias. A conservative staggered-grid Chebyshev multidomain method for compressible flows. *J. Comput. Phys.*, 125(1):244–261, 1996.

R. Kraichnan. Eddy viscosity in two and three dimensions. *J. Atmo. Sci.*, 33(8):1521–1536, 1976.

D. Kuzmin. Hierarchical slope limiting in explicit and implicit discontinuous Galerkin methods. *Journal of Computational Physics*, 257:1140–1162, 2014.

H. Luo, J. D. Baum, and R. Löhner. A Hermite WENO-based limiter for discontinuous Galerkin method on unstructured grids. *Journal of Computational Physics*, 225(1):686–713, 2007.

Y. Maday, S. M. O. Kaber, and E. Tadmor. Legendre pseudospectral viscosity method for nonlinear conservation laws. *SIAM Journal on Numerical Analysis*, 30(2):321–342, 1993.

S. Nagarajan, S. Lele, and J. Ferziger. Leading-Edge Effects in Bypass Transition. *J. Fluid Mech.*, 572: 471–504, 2007.

U. Piomelli, P. Moin, and J. H. Ferziger. Model consistency in large eddy simulation of turbulent channel flows. *Phys. Fluids*, 31(7):1884–1891, 1988. doi: 10.1063/1.866635.

S. Premasuthan, C. Liang, and A. Jameson. Computation of flows with shocks using the spectral difference method with artificial viscosity, I: basic formulation and application. *Computers & Fluids*, 98:111–121, 2014.

J. Qiu and C.-W. Shu. Runge-kutta discontinuous Galerkin method using WENO limiters. *SIAM Journal on Scientific Computing*, 26(3):907–929, 2005.

A. Rault, G. Chiavassa, and R. Donat. Shock-vortex interactions at high mach numbers. *Journal of Scientific Computing*, 19(1-3):347–371, 2003.

J. Shen, T. Tang, and L.-L. Wang. *Spectral methods: algorithms, analysis and applications*, volume 41. Springer Science & Business Media, 2011.

C. Shu and S. Osher. Efficient implementation of essentially non-oscillatory shock-capturing schemes. *J. Comput. Phys.*, 77(2):439–471, 1988.

G. A. Sod. A survey of several finite difference methods for systems of nonlinear hyperbolic conservation laws. *Journal of computational physics*, 27(1):1–31, 1978.

V. C. B. Sousa and C. Scalo. A unified Quasi-Spectral Viscosity (QSV) approach to shock capturing and large-eddy simulation. (in press at the Journal of Computational Physics), 2021.

V. C. B. Sousa and C. Scalo. A Legendre spectral viscosity (LSV) method applied to shock capturing for high-order flux-reconstruction schemes. *Journal of Computational Physics*, page 111157, 2022a. doi: https://doi.org/10.1016/j.jcp.2022.111157. URL `https://www.sciencedirect.com/science/article/pii/S0021999122002194`.

V. C. B. Sousa and C. Scalo. A unified Quasi-Spectral Viscosity (QSV) approach to shock capturing and large-eddy simulation. *Journal of Computational Physics*, 459: 111139, 2022b. ISSN 0021-9991. doi: https://doi.org/10.1016/j.jcp.2022.111139. URL `https://www.sciencedirect.com/science/article/pii/S0021999122002017`.

E. Tadmor. Convergence of spectral methods for nonlinear conservation laws. *SIAM Journal on Numerical Analysis*, 26(1):30–44, 1989.

E. Tadmor. Shock capturing by the spectral viscosity method. *Computer Methods in Applied Mechanics and Engineering*, 80(1-3):197–208, 1990.

N. Tonicello, G. Lodato, and L. Vervisch. Entropy preserving low dissipative shock capturing with wave-characteristic based sensor for high-order methods. *Computers & Fluids*, 197:104357, 2020.

E. F. Toro, M. Spruce, and W. Speares. Restoration of the contact surface in the HLL-Riemann solver. *Shock waves*, 4(1):25–34, 1994.

Z. J. Wang and H. Gao. A unifying lifting collocation penalty formulation including the discontinuous Galerkin, spectral volume/difference methods for conservation laws on mixed grids. *Journal of Computational Physics*, 228(21):8161–8186, 2009.

D. M. Williams, P. Castonguay, P. E. Vincent, and A. Jameson. Energy stable flux reconstruction schemes for advection–diffusion problems on triangles. *Journal of Computational Physics*, 250:53–76, 2013.

P. Woodward and P. Colella. The numerical simulation of two-dimensional fluid flow with strong shocks. *Journal of computational physics*, 54(1):115–173, 1984.

X. Zhang. On positivity-preserving high order discontinuous Galerkin schemes for compressible Navier–Stokes equations. *Journal of Computational Physics*, 328:301–343, 2017.

J. Zhu, J. Qiu, C.-W. Shu, and M. Dumbser. Runge–Kutta discontinuous Galerkin method using WENO limiters II: unstructured meshes. *Journal of Computational Physics*, 227(9):4330–4353, 2008.